

# Gap-Filling Mobile Radar Observations of a Snow Squall in the San Luis Valley

ANDREW A. ROSENOW

*Cooperative Institute for Mesoscale Meteorological Studies, University of Oklahoma, and  
NOAA/OAR/National Severe Storms Laboratory, Norman, Oklahoma*

KENNETH HOWARD

*NOAA/OAR/National Severe Storms Laboratory, Norman, Oklahoma*

JOSÉ MEITÍN

*Cooperative Institute for Mesoscale Meteorological Studies, University of Oklahoma, and  
NOAA/OAR/National Severe Storms Laboratory, Norman, Oklahoma*

(Manuscript received 1 November 2017, in final form 2 May 2018)

## ABSTRACT

On 24 January 2017, a convective snow squall developed in the San Luis Valley of Colorado. This squall produced rapidly varying winds at San Luis Valley airport in Alamosa, Colorado, with gusts up to  $12 \text{ m s}^{-1}$ , and an associated visibility drop to 1.4 km from unlimited in less than 10 min. This snow squall was largely undetected by the operational WSR-88D network because of the Sangre de Cristo Range of the Rocky Mountains lying between the valley and the nearest WSR-88D in Pueblo, Colorado. This study presents observations of the snow squall from the X-band NOAA X-Pol radar, which was deployed in the San Luis Valley during the event. These observations document the squall developing from individual convective cells and growing upscale into a linear squall, with peak radial velocities of  $15 \text{ m s}^{-1}$ . The environment conducive to the development of this snow squall is examined using data from the High-Resolution Rapid Refresh model, which shows an environment unstable to ascending surface-based parcels, with surface-based convective available potential energy (SBCAPE) values up to  $600 \text{ J kg}^{-1}$  in the San Luis Valley. The mobile radar data are integrated into the Multi-Radar Multi-Sensor (MRMS) mosaic to illustrate both the large improvement in detectability of this event gained from a gap-filling radar as well as the capability of MRMS to incorporate data from new radars designed to fill gaps in the current radar network.

## 1. Introduction

A snow squall, a convective mesoscale snowfall event characterized by a sudden increase in wind velocity, a sudden change in wind direction, and a sudden burst of snowfall, has long been known to be a significant hazard (Loisel 1909). Because of the threat that snow squalls pose to life and property, the National Weather Service (NWS) recently began issuing experimental, short-fuse warnings for snow squalls (NWS 2017). Snow squalls are relatively common in regions that experience lake-effect snow, as the squalls can form amid the lake-induced instability. Squalls also often form in association with lake-effect

mesovortices (e.g., Forbes and Merritt 1984; Pease et al. 1988). Convective snow squalls have also been observed across the United States and Canada outside of the favored lake-effect regions. Also known as snow bursts, snow squalls have been observed in a variety of places, including New England (Lundstedt 1993), the U.S. Midwest (Pettegrew et al. 2009), Canada (Milrad et al. 2011, 2014), and just east of the Rockies (Schultz and Knox 2007; Schumacher et al. 2010), though the number of cases of high-impact but limited-moisture cold season events in the literature is low (Milrad et al. 2011). These non-lake-effect squalls are difficult to predict, though Lundstedt (1993) and Milrad et al. (2011) provide some guidance on forecasting non-lake-effect snow squalls.

For phenomena that are difficult to predict, a robust observational network is important to ensure sufficient

---

*Corresponding author:* Andrew A. Rosenow, andrew.rosenow@noaa.gov

detection and warning capability for forecasters. Gaps and areas with poor coverage within operational radar networks, including the WSR-88D network, are therefore a significant issue. While the WSR-88D network provides good coverage over the eastern United States, the network has significant gaps in coverage in the western portion of the country owing to the more significant complex terrain, primarily associated with the Rocky Mountains (NRC 1995). This limited coverage has implications for detection of significant weather, including precipitation estimation (Maddox et al. 2002). This problem is compounded even more for events like snow squalls for which the ability to communicate the threat to the public has been historically challenging (DeVoi 2004).

Previous studies have shown benefits of installing radars to fill in gaps in operational radar networks, particularly using smaller, less expensive radars such as X-band radars. The Collaborative Adaptive Sensing of the Atmosphere test bed (CASA; McLaughlin et al. 2009) used a demonstration network of X-band radars to improve low-level radar coverage in Oklahoma. The CASA network was later moved to the Dallas–Ft. Worth metroplex in Texas to demonstrate the benefits of increased low-level radar coverage in an urban environment (Chandrasekar et al. 2013). Jorgensen et al. (2011) demonstrated improvements in warning ability for debris flows by placing a C-band radar near a mountainous area that had recently been impacted by a wildfire. Beck and Bousquet (2013) described the improvements in reflectivity and wind retrievals within the southern Alps in France as a result of X-band radars placed to cover terrain-induced gaps in the national radar network. Campbell and Steenburgh (2014) demonstrated the improvement in observation of orographically induced precipitation variation using an X-band mobile radar in Utah.

Here, mobile radar observations of a snow squall that developed in the San Luis Valley on 24 January 2017 are described. This event was largely missed by the operational radar network, and represents an example of the type of event that would benefit from the addition of gap-filling radars. These radar data are also used to illustrate the existing operational capability to integrate gap-filling radar data with WSR-88D radar data. The rest of the paper is organized as follows: section 2 describes the data and methodology used in this study. Section 3 describes the synoptic setting under which the squall developed. Section 4 describes the mobile radar data collected during this event. Section 5 examines surface observations during the snow squall passage and quantifies the number of similar events at the surface station in the past. Section 6 presents the results of merging the mobile radar data into an operational radar mosaic to facilitate the presentation of gap-filling

TABLE 1. NOXP operational parameters for this study.

Wavelength	3 cm
Beamwidth	0.9°
Pulse width	50 $\mu$ s
Scanning VCP	0.5°, 0.9°, 1.3°, 1.8°, 2.4°, 3.1°, 4.0°, 5.1°, 6.4°, 8.0°, 10.0°, 12.5°
Volume scan time	~4 min, 10 s
Peak power	250 kW
Operational range	130 km
Ground clutter filter	SIGMET “GMAP” notch filter (Siggia and Passarelli 2004)

radar data to end users. Finally, section 7 presents the conclusions of the paper.

## 2. Data and methodology

Data from this project were collected as part of the Upper Rio Grande Water Resource Project. This project was a collaboration between the National Severe Storms Laboratory, the state of Colorado, and the city and county of Alamosa, Colorado. The goal of the project was to assess the possible improvements in quantitative precipitation estimation (QPE) in the Rio Grande and Conejos River basins by improving radar coverage in the San Juan Mountains, where these rivers are sourced. For this project, the NOAA X-pol (NOXP) radar was deployed at San Luis Valley Regional Airport (KALS, elevation 2298 m). A summary of the NOXP specifications is presented in Table 1.

The gap in radar coverage in the San Luis Valley is due to a combination of distance from radars and topography. Figure 1a shows the location of KALS relative to the WSR-88Ds in Colorado, and a topographic map of the San Luis Valley is shown in Fig. 1b. The KPUX (Pueblo, Colorado) radar is northeast of Fig. 1b, meaning the low levels of the San Luis Valley are blocked by the Sangre de Cristo Range surrounding the northeast portion of the valley. At its location at KALS, NOXP was located roughly in the middle of the San Luis Valley, approximately 35 km from the nearest mountains to the east and west. Here, the radar had good visibility of the entire San Luis Valley and adjacent mountains, with the exception of beam blockage to the northeast caused by buildings on the airport grounds.

The radar was operated in a modified version of volume coverage pattern 12 (VCP 12; Brown et al. 2005) that removed the top two elevation scans (15.8° and 19.5°), but maintained a similar volume scan time of about 4 min and 10 s. The radar was operated continuously during precipitation events in the San Juan Mountains, including during the event presented here. Because of the significant, prolonged cold in the San

Luis Valley during winter, the radar had intermittent issues<sup>1</sup> with its transmitter. The transmitter problems primarily affected dual-polarization variables, such as differential reflectivity  $Z_{DR}$  and correlation coefficient  $\rho_{hv}$ . Single-polarization variables, specifically horizontal equivalent radar reflectivity factor  $Z_{HH}$  (hereafter reflectivity) and radial velocity  $V$  were less affected by the transmitter overall, and the single-polarization moments from this specific case look reasonable. While the single-polarization variables will be discussed in this study, dual-polarization radar variables will not be presented here out of an abundance of caution.

In addition to data from NOXP, this study also utilizes data from the KALS automated surface observing system (ASOS), as well as model output from the High-Resolution Rapid Refresh (HRRR) model (Smith et al. 2008). HRRR output data are taken from the 2000 UTC 24 January model run. The HRRR model was used because of its relatively fine horizontal resolution, a necessity with the complex terrain surrounding the San Luis Valley.

### 3. Synoptic summary

The snow squall event occurred as synoptic-scale ascent and the attendant cyclone were departing southern Colorado. At 1200 UTC 24 January, approximately 9 h prior to the arrival of the snow squall in Alamosa, a 500-hPa trough was located over Utah, shown in Fig. 2a. The trough then moved to the east over the course of the day. Over Colorado, relatively light westerly flow at 500 hPa ( $12.5 \text{ m s}^{-1}$  at Denver) was advecting cold air aloft, with 500-hPa temperatures of  $-27^\circ\text{C}$  at Denver, Colorado;  $-30^\circ\text{C}$  at Grand Junction, Colorado; and  $-31^\circ\text{C}$  at Salt Lake City, Utah. In association with the upper-level trough, a 994-hPa surface cyclone was located near the Colorado–Kansas border (Fig. 2b). While cold air advection was occurring amid northerly flow across the eastern plains of Colorado west of the cyclone, the mountains of the Sangre de Cristo Range blocked the San Luis Valley from the cold air that was surging southward across the eastern plains of Colorado.

<sup>1</sup> The intermittent transmitter problems manifest themselves in several radar variables, including a constant  $\rho_{hv}$  of 1 for every gate and declining reflectivities ( $Z_{HH}$ ) with time. These symptoms are not present in the data for this case. Moreover, small errors in reflectivity magnitude would not materially affect this study as long as the gate-to-gate relative magnitudes of reflectivity, and therefore the shape of relevant features, are preserved, something that was true even in data from other time periods affected by the transmitter issue. We also have confidence in the measured velocities due to the radar-measured winds with the squall presented here ( $15 \text{ m s}^{-1}$ ) being close to wind gusts observed on the ground ( $12 \text{ m s}^{-1}$ ) around the same time as the radar measurement.

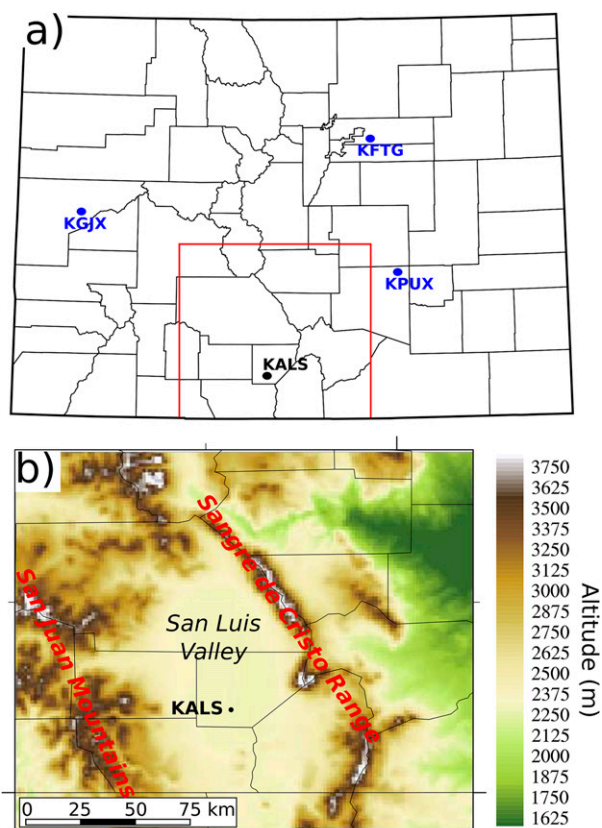


FIG. 1. (a) Map of the state of Colorado. Blue dots indicate locations of NWS operational WSR-88Ds. The black dot indicates the location of San Luis Valley Regional Airport (KALS). The red box indicates a zoom-in area. (b) Topographic map (shaded) of the San Luis Valley for the region indicated in the red box in (a). Elevation (m) is shaded. Labels indicate geographic features of note.

Thus, winds were light at KALS, and remained so even as winds across the eastern plains of Colorado strengthened.

At 0000 UTC 25 January, the upper-level trough axis at 500 hPa was located near the Colorado–Kansas border, having moved east during the day (Fig. 2c). The 500-hPa temperature at Denver was  $-30^\circ\text{C}$ , which was  $4^\circ$  colder than at 1200 UTC. Midlevel winds continued to be light, with 500-hPa winds at Denver of  $10 \text{ m s}^{-1}$  out of the west-northwest. As the trough moved east, the cyclone had also moved to the east into eastern Kansas and deepened slightly to 992 hPa (Fig. 2d). The strong surface flow remained confined to the eastern plains of Colorado, however, as KALS again reported light winds.

The upper-level trough can also be seen in water vapor imagery. Figure 3 shows the GOES-West water vapor image about 3 h prior to the snow squall. The warm colors, indicating drier air aloft, show the base of the trough off the coast of California into northern

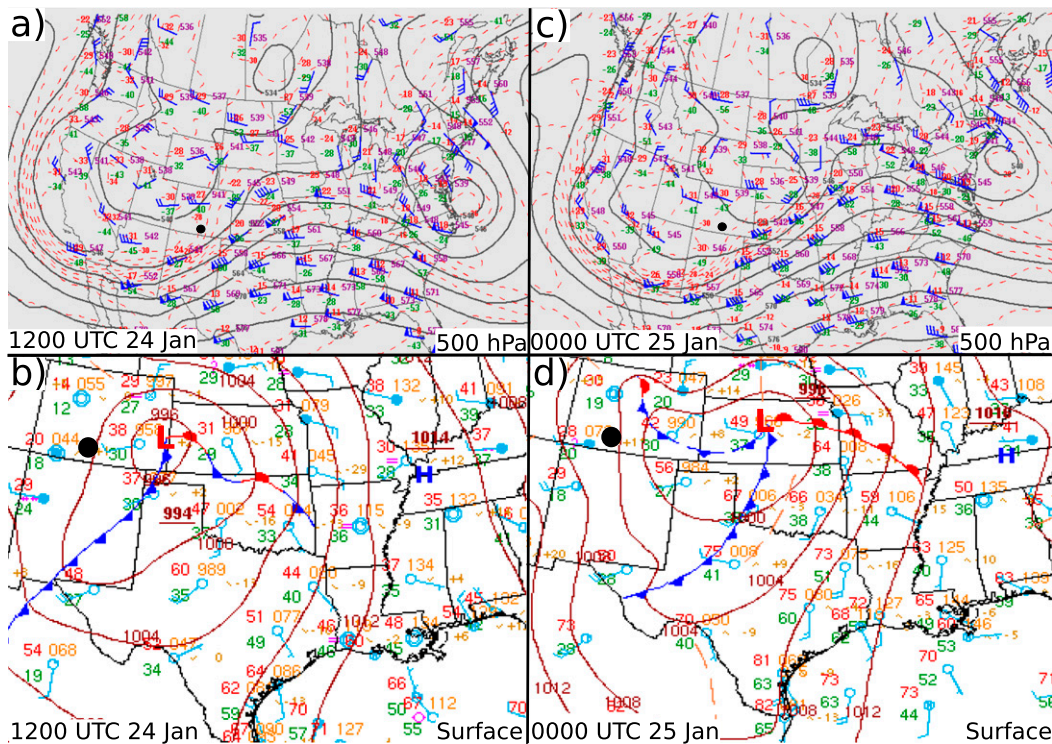


FIG. 2. (a) 500-hPa observations and analysis valid at 1200 UTC 24 Jan 2017. (b) Surface observations and NOAA Weather Prediction Center analysis valid at 1200 UTC 24 Jan 2017. (c) As in (a), but for 0000 UTC 25 Jan 2017. (d) As in (b), but for 0000 UTC 25 Jan 2017. The black dot in each panel indicates the location of KALS.

Mexico, southern Arizona, and southern New Mexico. The colder colors over western Colorado likely indicate the location of the trough axis. As seen in Figs. 2a and 2c, this trough was moving to the east, bringing the trough axis over the San Luis Valley.

To better examine the state of the atmosphere in the San Luis Valley, an HRRR sounding from 2000 UTC 24 January for KALS is presented in Fig. 4a. This model sounding is from about 1 h before the snow squall impacted KALS. The model sounding features a low tropopause around 400 hPa caused by the trough overhead. Strong (greater than  $25 \text{ m s}^{-1}$ ) winds were confined to the stratosphere, with winds within the troposphere generally under  $15 \text{ m s}^{-1}$ . Winds in the troposphere were out of the west through the depth of the sounding, with only minor variations in speed and direction. The thermal and moisture profile in the troposphere consists of two main layers. Near the surface, a well-mixed boundary layer extended up to about 650 hPa. Above that, the atmosphere was unstable for saturated ascent up to the tropopause. The dashed line in Fig. 4a indicates the path of the most unstable parcel, which was sourced from the well-mixed boundary layer and becomes unstable on reaching saturation.

The model indicated the presence of surface-based instability throughout the San Luis Valley, as shown by

the 2000 UTC surface-based convective available potential energy (SBCAPE) plot from the HRRR shown in Fig. 4b. Surface-based convective inhibition (SBCIN) in the model was near zero across the valley in the model (not shown). The SBCAPE magnitudes were maximized within the San Luis Valley to the northeast of KALS with peak values near  $600 \text{ J kg}^{-1}$ , and a northwest–southeast axis of SBCAPE values above  $300 \text{ J kg}^{-1}$  across the northern and eastern portions of the San Luis Valley.

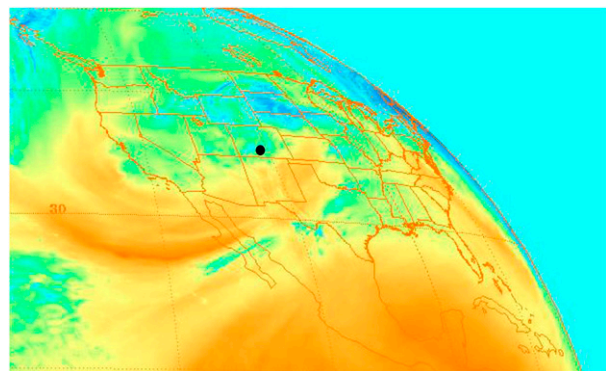


FIG. 3. GOES-West water vapor imagery from 1800 UTC 24 Jan 2017. The dot indicates the location of KALS.

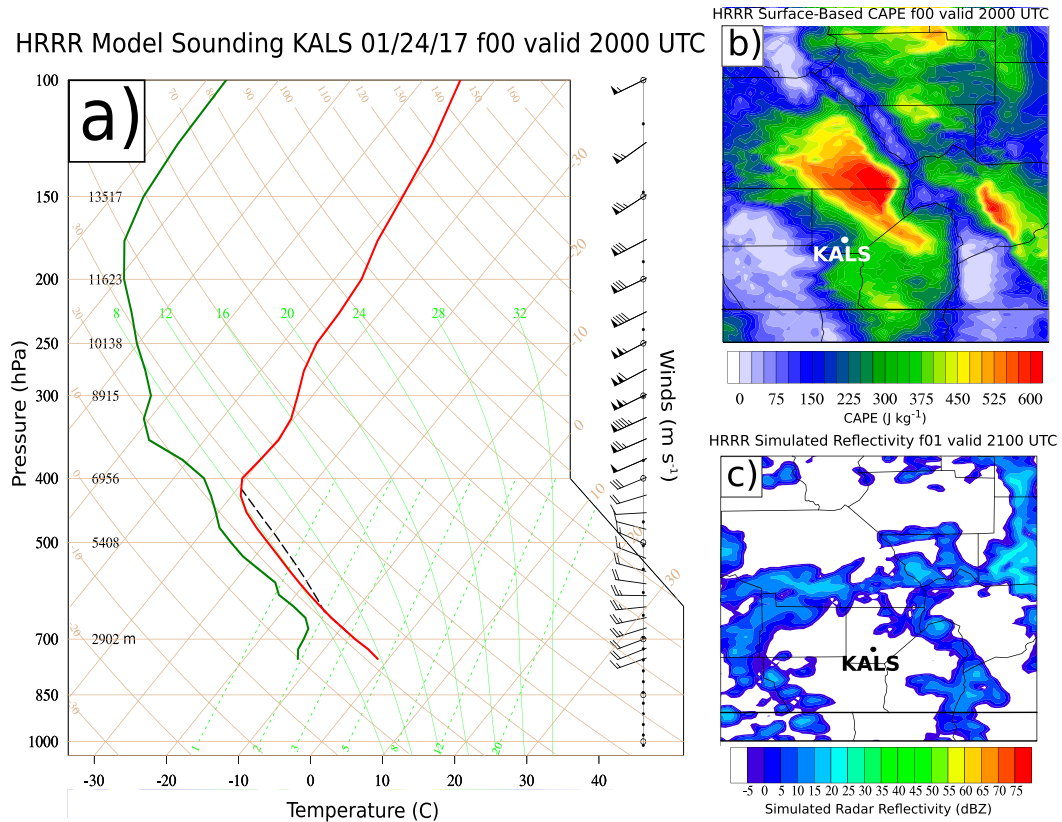


FIG. 4. (a) HRRR model sounding valid at KALS at 2000 UTC for the 2000 UTC HRRR run. Winds are in  $\text{m s}^{-1}$  with short lines on wind barbs indicating  $2.5 \text{ m s}^{-1}$ , a long line indicating  $5 \text{ m s}^{-1}$ , and a flag indicating  $25 \text{ m s}^{-1}$ . The dashed line indicates the most unstable parcel path. (b) Surface-based convective available potential energy (CAPE) from the 2000 UTC HRRR 0-h forecast on 24 Jan 2017. (c) HRRR model-simulated S-band radar reflectivity 1-h forecast valid at 2100 UTC 24 Jan 2017.

To illustrate the model's response to the environment characterized in Figs. 4a and 4b, the HRRR 1-h forecast-simulated radar reflectivity valid at 2100 UTC (1 h after Figs. 4a and 4b) is shown in Fig. 4c. The 2000 UTC 1-h forecast HRRR plot is used here as it was close to the event, where the model should have the closest possible representation of the environment, while also giving the model time to initiate the convection antecedent to the snow squall. Almost all of the precipitation in the model at 2100 UTC near KALS was confined to the high terrain surrounding the San Luis Valley. Despite the relatively large SBCAPE values in the model for the San Luis Valley in Fig. 4b at 1 h prior, the model only generated a few very light showers (simulated reflectivities of 10 dBZ or less) over the northwestern portion of the San Luis Valley. As will be shown in the following section, this time period corresponded to the organization and strengthening of the snow squall, something completely absent in the HRRR model forecast. Previous HRRR runs examined as part of this study, back to the 1500 UTC 6-h

forecast (not shown), likewise did not show any significant precipitation within the San Luis Valley at 2100 UTC.

#### 4. Radar observations

This section describes the NOXP observations of the snow squall. There are several important considerations when comparing X-band radar measurements from NOXP with S-band radars, such as the WSR-88Ds. These differences are apparent in both rainfall (e.g., Matrosov et al. 2006; Chandrasekar et al. 2006; Junyent and Chandrasekar 2016) and snowfall (Matrosov et al. 2009). The most relevant factors for convective snow include stronger attenuation at the X band in the presence of liquid water (whether caused by melting particles or supercooled water) and the possibility for larger particles/aggregates to lie in the Mie scattering regime for X-band radars. There are also differences with dual-polarization products not considered here, such as stronger phase shift at the X band and a varying

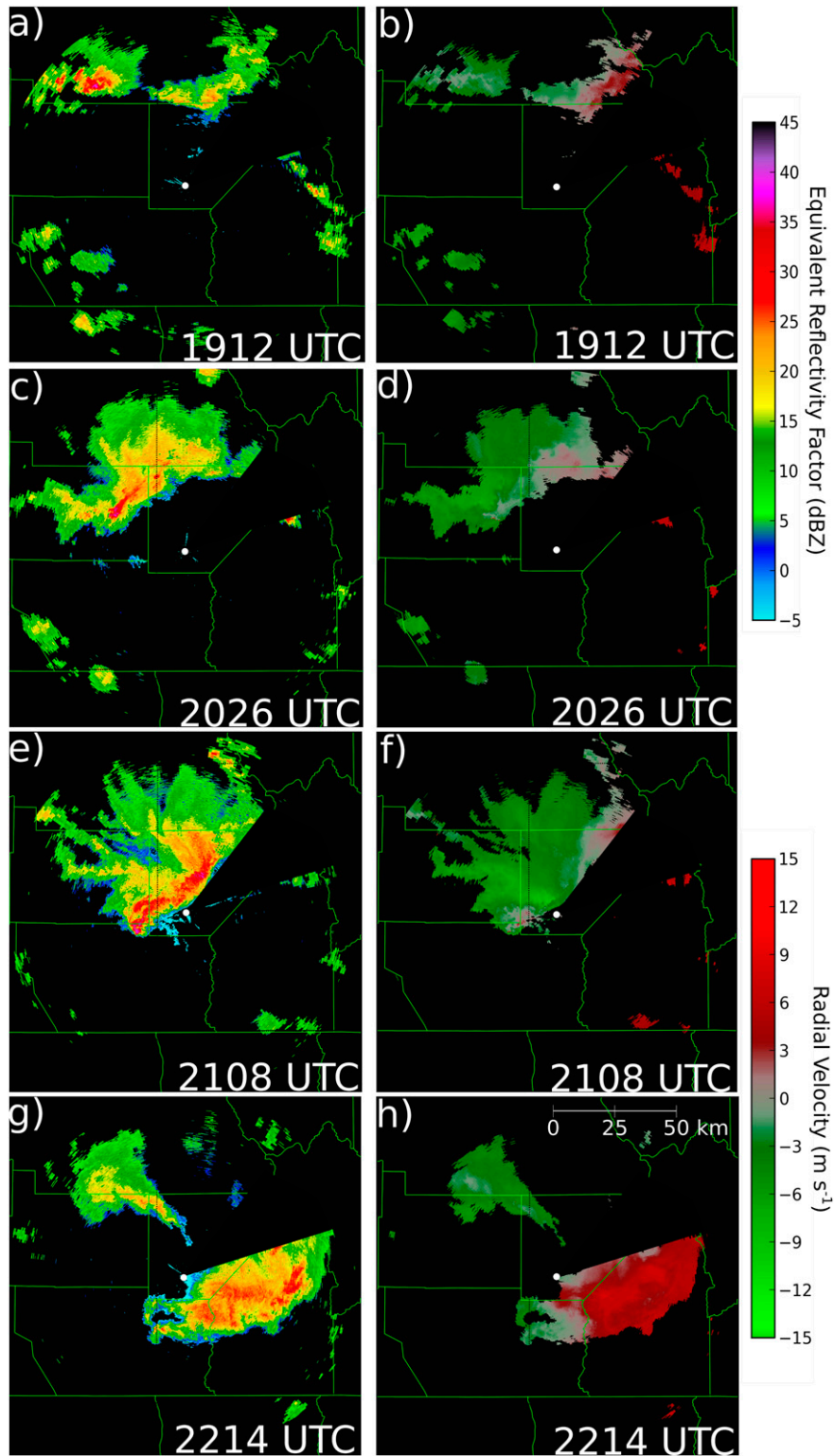


FIG. 5. NOXP (a),(c),(e),(g) equivalent radar reflectivity factor (dBZ) and (b),(d),(f),(h) radial velocity ( $\text{m s}^{-1}$ ). All images are from the  $0.5^\circ$  elevation angle. Times are indicated on each image.

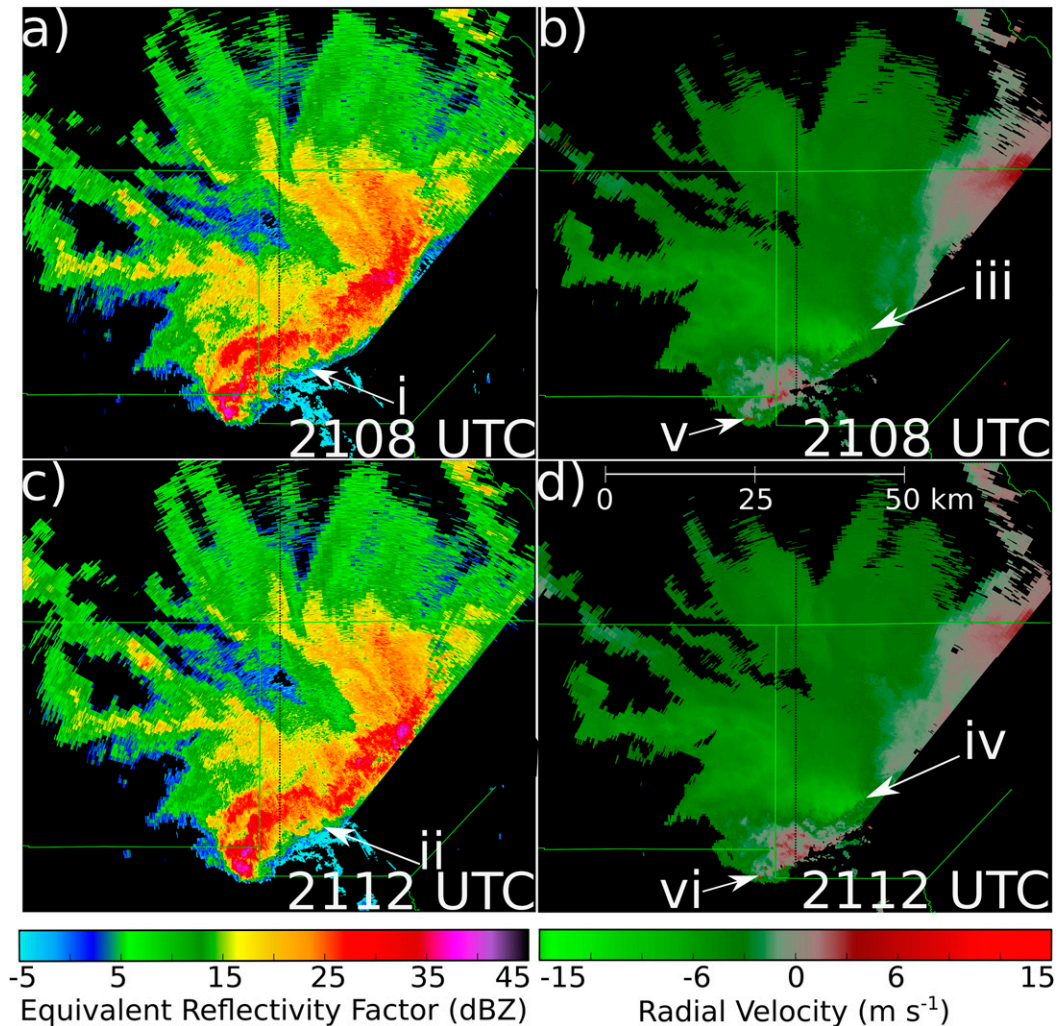


FIG. 6. (a) NOXP reflectivity and (b) radial velocity at 2108 UTC 24 Jan 2017. Roman numerals indicate features discussed in the text. (c),(d) As in (a),(b), but for 2112 UTC.

difference in  $Z_{DR}$  based on the particle size distribution (Chandrasekar et al. 2006).

From its position at the airport, NOXP was able to observe the entire life cycle of the snow squall, and these data are summarized in Fig. 5. Both columns present plan position indicator (PPI) plots from the  $0.5^\circ$  elevation scans. Scans to the northeast of the radar were blocked by hangars at the airport, which caused that sector to contain either a gap in echoes or reflected echoes of precipitation that were actually located to the southwest of the radar. To simplify the interpretation of the radar images in this study, we have removed the bad data from this northeastern sector in Figs. 5 and 6.

The NOXP reflectivity plot in Fig. 5a valid at 1912 UTC 24 January shows that a number of snow showers were in the radar's domain. The snow showers were located mostly over the higher terrain surrounding

the San Luis Valley, with the most intense snow showers northwest of the valley. Maximum reflectivity values in the strongest cells were near 35 dBZ. These convective cells were the beginning of the snow squall that eventually traversed the San Luis Valley. Radial velocities at this time (Fig. 5b) were generally  $5 \text{ m s}^{-1}$  or less.

Over the next hour, the individual convective cells began to merge into a larger and more organized convective system. In the reflectivity PPI at 2026 UTC (Fig. 5c), the strongest echoes become linear and at the front of a southeasterly-propagating area of precipitation. The most intense echoes were of similar magnitude to the incipient convective cells, however, some large snow particles may be in the Mie scattering regime at X-band radar wavelengths if significant aggregation was occurring. Thus, it may not be possible to infer a change in precipitation intensity solely based on reflectivity

changes, especially because of the lack of reliable dual-pol measurements in this study.

As the reflectivity signature became more organized, similar changes were apparent in the developing squall's velocity signature (Fig. 5d). Stronger inbound velocities, up to  $10 \text{ m s}^{-1}$ , were advancing from the northwest toward the southeastern leading edge of the radar echoes. The most intense reflectivities were located just ahead of these stronger velocities in an area of enhanced convergence, and that convergence is known to be important to initiation and sustainment of convection (Wilson and Schreiber 1986).

Over the next half hour the squall reached maturity, as evidenced by the line of reflectivity values greater than 25 dBZ as well as the large reflectivity gradient on the leading edge of the convection (Fig. 5e). At this time (2108 UTC), the intense line of the snow squall was approximately 50 km in length from southwest to northeast, and the line of highest reflectivities was about 6 km wide at its widest point. Peak reflectivities were above 40 dBZ. The sharp cutoff on the east side of the precipitation is due to beam blockage caused by buildings on the airport grounds.

Also at 2108 UTC, the radial velocities associated with the squall were near their maximum magnitudes (Fig. 5f). Once again, the strongest radial velocities, here up to  $15 \text{ m s}^{-1}$ , were collocated with the strongest reflectivities. In subsequent scans the squall's outflow undercut and outran the leading-edge convective echoes, and the squall began to weaken.

By 2214 UTC, the snow squall had moved past the radar in Alamosa and was located over the eastern portion of the San Luis Valley. The linear maximum in reflectivity was no longer present by this point, with the exception of a small area of enhanced reflectivity on the eastern edge of the precipitation; this small maximum may have been due to enhanced low-level convergence and upslope flow along the mountains at the eastern edge of the San Luis Valley (Fig. 5g).

Measured velocities at 2214 UTC were weaker, with peak radial velocities up to  $12.5 \text{ m s}^{-1}$  (Fig. 5h). The radial velocity maxima were associated with a secondary surge of outflow, as the primary outflow surge near the front of the precipitation in Fig. 5f moved beyond the front of the convection in the intervening hour. After this time, the radial velocities would continue to weaken because of the cessation of the convection associated with the squall and the associated drop in convective outflow, but a large area of light snow persisted to the southeast of KALS.

Figure 6 shows zoomed-in radar images from two consecutive  $0.5^\circ$  elevation scans close in time to the peak intensity of the snow squall. Feature i in Fig. 6a shows the edge of the gust front associated with the

squall. This gust front had previously moved ahead of the leading edge of the convection, initiating new convection along the gust front northeast of feature i. At this time, only the portion of the gust front's fine line at i was still visible. This changed within four minutes, as new convective cells developed along the gust front, indicated as feature ii in Fig. 6c. Along the leading edge of the gust front, misovortices were present, indicated as features iii and iv in Figs. 6b and 6d. These misovortices were most prevalent around this portion of the squall's life cycle as the squall's outflow was maximized, and the squall's proximity to the radar meant the relatively narrow radar gates could more effectively resolve the features. There was also a larger mesovortex at the southwest end of the squall, labeled as features v and vi in Figs. 6b and 6d, respectively. The circulation appeared on the 2047 UTC scan and was no longer on radar after the 2124 UTC scan. It is possible that the circulation was still present after 2124 UTC and had simply moved far enough ahead of the precipitation to no longer be detected by the radar.

## 5. Surface observations

### a. Snow squall

A summary plot of surface observations from KALS on 24 January 2017 is presented in Fig. 7. During the early afternoon through around 2030 UTC, conditions at KALS were quiescent as temperatures warmed from  $-5^\circ\text{C}$  at 1800 UTC to  $+1^\circ\text{C}$  at 2030 UTC with winds generally out of the east at  $2\text{--}3 \text{ m s}^{-1}$ . This changed after 2050 UTC, when winds began to strengthen up to  $5\text{--}6 \text{ m s}^{-1}$  while becoming southwesterly, likely in response to low pressure perturbations associated with convection north of KALS at that time. At 2119 UTC, the KALS ASOS registered passage of the squall's gust front, and pressure rose from 1000 hPa prior to passage to a 1002-hPa postgust front. Simultaneously, the winds became northwesterly, then northerly, and increased to  $8 \text{ m s}^{-1}$  sustained with gusts registered up to  $11 \text{ m s}^{-1}$ . The temperature–dewpoint spread narrowed from its presquall maximum of  $10^\circ$  to  $2^\circ\text{C}$  after gust front passage. As precipitation and gusty winds arrived with the snow squall, visibility quickly dropped from at least 16 to 1.4 km during the span of 15 min, and the visibility remained less than 2.5 km for more than 30 min, with a minimum visibility of 0.4 km. Once the precipitation ended, visibility slowly returned to more than 16 km and winds calmed to  $2\text{--}3 \text{ m s}^{-1}$  from the east and southeast.

Later in the evening, KALS was affected by multiple additional precipitation events. Light snow, which occurred from 2330 UTC 24 January to 0030 UTC 25 January, and

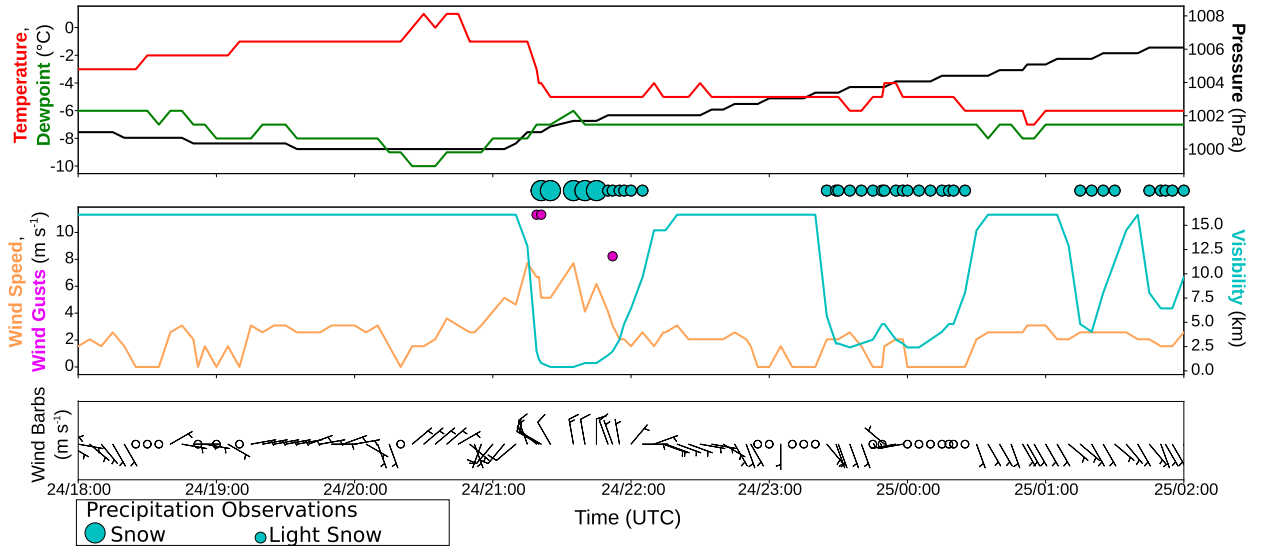


FIG. 7. Plot of surface observations from San Luis Valley Regional Airport's ASOS, KALS. (top) Temperature ( $^{\circ}\text{C}$ , red), dewpoint ( $^{\circ}\text{C}$ , green), and pressure (hPa, black). (middle) Wind speed (orange line,  $\text{m s}^{-1}$ ), wind gusts (purple dots,  $\text{m s}^{-1}$ ), visibility (cyan line, km), and ASOS precipitation observations (cyan circles). (bottom) Wind barbs, with short and long bars representing  $2.5 \text{ m s}^{-1}$  and  $5 \text{ m s}^{-1}$ , respectively.

again between 0115 and 0200 UTC 25 January, did not have similar impacts on the low-level wind field as these snow showers were more stratiform in nature. Because of the lack of winds and lighter snowfall rates compared to the snow squall, the visibility never dropped below 2.5 km during these events. This event did not produce heavy snow accumulations, with KALS reporting 4.6 cm in new snow accumulation on 24 January, some of which was associated with the later snowfall and not the squall itself (NCDC 2018).

### b. Similar events at KALS

The historical data from the KALS ASOS can be used to estimate how often events similar to this snow squall occur. For this purpose, 5476 days' worth of surface observations were processed. These surface observations were collected from 6 February 2003 to 6 February 2018. The first analysis performed was to find days with comparable sensible impacts to the snow squall by searching for observations at KALS with winds (gusts or sustained) above  $10 \text{ m s}^{-1}$ , visibility at or below 0.8 km, and an observation of snow. Instead of counting observations exceeding these criteria, the number of days with at least one observation exceeding the criteria was calculated. A particular event may be double counted if it happened to span over the end of a day in UTC, but this methodology eliminates counting issues related to the varying ASOS observation interval. Over the 15 years of data, there were 52 days with observations meeting these criteria, or an average of  $3.5 \text{ days yr}^{-1}$ .

The aforementioned criteria can be met by other causes beside convective snow squalls, such as cyclones. To find cases more similar to this snow squall event, the observations were analyzed again, adding the additional condition that sustained winds must have increased by  $5 \text{ m s}^{-1}$  in the hour prior to the observation meeting the visibility, weather, and wind criteria. With the addition of the wind increase to the criteria, there were 17 days in the record meeting the criteria, an average of  $1.1 \text{ days yr}^{-1}$ ; 1 of these 17 days is the day of the snow squall described in this paper. Further restricting the criteria to require the same  $5 \text{ m s}^{-1}$  increase in winds to occur in the prior 30 min reduces the number of matching days to 8, or about 1 day every other year. These 8 days do not include the 24 January 2017 event, as the  $5 \text{ m s}^{-1}$  increase in sustained winds took about 45 min to occur at KALS during that event.

This analysis suggests that events of similar impacts to this snow squall happen at KALS about once a year on average. Whether the other events were similar convective snow squalls or other meteorological setups, these other events would suffer from the same operational observation deficiency that will be demonstrated in the next section.

## 6. MRMS radar mosaic

This section will examine the available radar data for the snow squall event from the operational WSR-88D network using the Multi-Radar Multi-Sensor (MRMS; Zhang et al. 2016) radar mosaic. The MRMS suite was

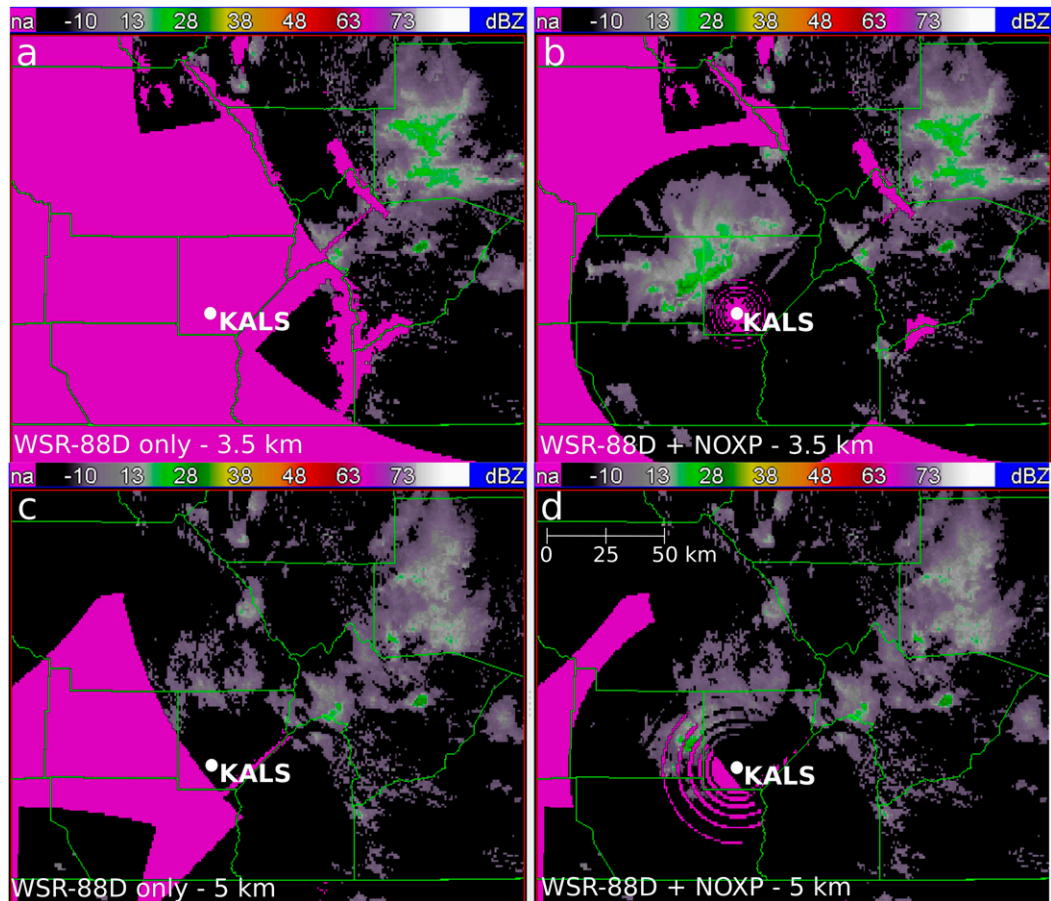


FIG. 8. Radar composite CAPPI plots created with the Multi-Radar Multi-Sensor software package valid at 2402 UTC 24 Jan 2017. Purple indicates areas with no radar coverage by any radar in the mosaic. (a) A mosaic consisting only of data from WSR-88Ds, and is valid at 3.5 km MSL. (b) A mosaic of WSR-88D data and NOXP data valid at 3.5 km. (c) As in (a), but valid at 5 km. (d) As in (b), but valid at 5 km MSL.

developed at the National Severe Storms Laboratory and the University of Oklahoma and is run operationally at the National Centers for Environmental Prediction. MRMS not only incorporates WSR-88D data in its mosaic, but also data from a variety of other radar systems; the algorithm used to merge the radars together is described in Lakshmanan et al. (2006). This capability was used to merge the data from NOXP into the WSR-88D mosaic. The operational MRMS mosaic has 1-km horizontal spatial resolution and is updated every 2 min; this same 1-km grid resolution is used here.

Figure 8a contains mosaicked WSR-88D radar data valid at 2042 UTC at 3.5 km MSL, around 1 km AGL for the San Luis Valley. This plot represents the entirety of radar data available at this altitude in the WSR-88D network. Almost the entire San Luis Valley and the San Juan Mountain range are in the purple regions, which indicates that the radar network cannot detect anything at that altitude. When the NOXP data are added to the

mosaic in Fig. 8b, the data from NOXP clearly show the presence of the snow squall. This mosaic is valid about half an hour prior to the squall impacting KALS.

When looking at a higher altitude, 5 km MSL (or around 2.5 km AGL for the San Luis Valley), the WSR-88D network detected some of the precipitation with the snow squall, as shown in Fig. 8c. While there are echoes over the San Luis Valley at 5 km, the echoes were weak (<20 dBZ) and disorganized, and gave no indication of the actual strength or true organization of the precipitation. When the NOXP data are added in Fig. 8d, NOXP allowed the detection of more precipitation at 5 km. While the structure of the snow squall is less obvious at this altitude, the NOXP-inclusive mosaic still shows that the system is larger, more organized, and more intense than the WSR-88D observations indicated. The purple rings in the echoes in Figs. 8b and 8d are mosaicking artifacts caused by gaps between elevation scans in the NOXP volume coverage pattern.

This pattern is consistent across other times analyzed, which are not shown here. The mosaics using WSR-88D data exclusively missed almost all of the precipitation associated with the snow squall. The precipitation detected by WSR-88Ds was weak, scattered, and only at the top of the squall. Not only does the addition of the data from NOXP ensure the snow squall is in the mosaic, but the data from NOXP also integrated well into the mosaic, with the boundary between NOXP and WSR-88D data generally not being obvious.

## 7. Discussion and conclusions

This study presents a snow squall in Colorado's San Luis Valley, a high-elevation valley surrounded by mountains that block the operational WSR-88D network from providing adequate radar coverage. The snow squall was not substantially detected by the operational WSR-88D network. Because of the intensity of the event not being forecast and not being detected by operational data networks beforehand, no information about the squall and its potential impacts in Alamosa was available until after the squall arrived and showed up in the KALS ASOS data.

The snow squall formed in an environment with HRRR model SBCAPE values up to  $600 \text{ J kg}^{-1}$  and surface dewpoint depressions of  $10^\circ\text{C}$ . The instability enabled the development of vigorous convective snow showers, and the relatively large temperature–dewpoint spread contributed to the formation of a cold pool that enabled the convective elements to consolidate into a line. This event reinforces the importance of monitoring parameters such as CAPE when convective snow showers are forecast. This event also serves as a reminder that numerical models provide information that the environment is favorable for convective events, but they absolutely cannot substitute for observation of the timing and location of the ensuing convection. While the HRRR produced an instability distribution that is consistent with the development of the snow squall, the model did not actually capture the squall's development (Fig. 4c). The 3-km grid spacing of the HRRR is likely insufficient to represent the critical upscale growth from small individual convective cells, especially when coupled with the paucity of observations in the San Luis Valley.

The presence of NOXP allowed the life cycle of the snow squall to be documented. The squall formed as convective snow showers that developed near and over mountains in the northwest portion of the San Luis Valley grew upscale into a linear convective feature. As this convective line developed and matured, measured Doppler velocities increased to a maximum value of  $15 \text{ m s}^{-1}$ . This stronger outflow began toward the rear of

the developing squall's precipitation and propagated toward the leading edge of the precipitation. As the stronger outflow reached the front of the squall, the squall reached its peak intensity. Once the outflow outran the front edge of the squall, Doppler velocities and reflectivities diminished as the squall's leading-edge convection was undercut by potentially colder air, likely reducing or eliminating surface-based instability. The radar detected a number of horizontal circulations, including a persistent mesovortex on the end of the squall and a number of misovortices along the gust front. The presence of misovortices is consistent with studies that reported similar features on thunderstorm gust fronts (e.g., Friedrich et al. 2005), and sea/lake-effect snow (e.g., Inoue et al. 2011; Steiger et al. 2013; Mulholland et al. 2017).

As the squall impacted the airport, the ASOS recorded the changes in sensible weather at the airport. Of note, the squall impacted winds both before its arrival because of the squall's inflow, as well as after its arrival due to the squall's outflow. These changes would not be possible to anticipate without knowledge of the snow squall's existence, and thus were a danger to transportation interests, such as aircraft operating out of this commercial airport. Additionally, the sudden decrease in visibility at KALS, driven by the convectively induced snowfall rate and winds, was likewise unable to be anticipated without knowledge of the existence of the snow squall. While the overall snowfall amount was not particularly heavy, the heavy initial burst of snowfall also created rapidly changing road and runway conditions. From the analysis of 15 years' worth of observations at KALS, days with similar impacts (winds over  $10 \text{ m s}^{-1}$  sustained after increasing by  $5 \text{ m s}^{-1}$  within the previous hour, visibility at or below 0.8 km, and snow falling) occur about once per year on average.

The data from NOXP were merged into a mosaic with WSR-88D data using the MRMS software. This capability to merge additional radars into the preexisting NWS radar mosaic allows these additional radar data from gap-filling radars to be used in a number of applications, including forecasting, nowcasting, and model evaluation. Integrating these data into MRMS also would allow the generation of the MRMS suite of products related to QPE, severe weather, winter weather, and more to be performed using gap-filling radar data. Additionally, the flexibility of MRMS to integrate data from non-WSR-88Ds means alternative radar systems could be used in an operational setting with relative ease by the NWS and the broader Weather Enterprise.

While this case provides another example of the benefits of gap-filling radars, deploying these radars is not always viable for economic or logistical reasons. One potential area of research would be to use this case

alongside other similar events to improve predictability of these types of events. A better understanding of these types of events, combined with new forecast tools such as the GOES-R series of geostationary satellites and improvements in the HRRR and other convection-allowing models, could mitigate some of the problems associated with gaps in the operational radar network where gap-filling radars are not economically justifiable. In this case specifically, a well-designed, high-resolution numerical simulation could lead to insight into the processes that led to this squall that cannot be ascertained in the data-sparse San Luis Valley beyond what is possible from NOXP data. Nevertheless, while these tools may be helpful in radar-deficient regions, they cannot replicate the benefits of expanded radar coverage, especially in the Intermountain West. Additional future work includes using these NOXP data or other gap-filling data to improve quantitative precipitation estimation in regions poorly served by the current radar network to provide a quantifiable benefit to the installation of more permanent gap-filling radars.

*Acknowledgments.* Funding for this work was provided by the Colorado Department of Natural Resources and the city and county of Alamosa, Colorado. The authors thank Joe Busto of the Colorado DNR as well as Dustin Allinger from San Luis Valley Airport. Funding was provided by NOAA/Office of Oceanic and Atmospheric Research under NOAA–University of Oklahoma Cooperative Agreement NA11OAR4320072, U.S. Department of Commerce. The authors thank Paul Wolyn, Paul Schlatter, and Mike Meyers of the National Weather Service for helpful discussions on events within radar gaps in Colorado. HRRR data used in this study were obtained from the University of Utah MesoWest HRRR archive (Blaylock et al. 2017). Surface data from KALS were courtesy of the University of Utah's MesoWest archive (Horel et al. 2002). Plots of NOXP data were created using the Python ARM Radar Toolkit (Py-ART; Helmus and Collis 2016). Surface analyses used in Fig. 2 are courtesy of NOAA's Weather Prediction Center, and upper-air analyses are courtesy of NOAA's Storm Prediction Center. Water vapor imagery in Fig. 3 is from NCDC's GIBBS service (Knapp 2008). The authors thank Terry Schuur, Russ Schumacher, and three anonymous reviewers for providing helpful comments on the manuscript.

#### REFERENCES

- Beck, J., and O. Bousquet, 2013: Using gap-filling radars in mountainous regions to complement a national radar network: Improvements in multiple-Doppler wind syntheses. *J. Appl. Meteor. Climatol.*, **52**, 1836–1850, <https://doi.org/10.1175/JAMC-D-12-0187.1>.
- Blaylock, B. K., J. D. Horel, and S. T. Liston, 2017: Cloud archiving and data mining of High-Resolution Rapid Refresh forecast model output. *Comput. Geosci.*, **109**, 43–50, <https://doi.org/10.1016/j.cageo.2017.08.005>.
- Brown, R. A., V. T. Wood, R. M. Steadham, R. R. Lee, B. A. Flickinger, and D. Sirmans, 2005: New WSR-88D volume coverage pattern 12: Results of field tests. *Wea. Forecasting*, **20**, 385–393, <https://doi.org/10.1175/WAF848.1>.
- Campbell, L. S., and W. J. Steenburgh, 2014: Finescale orographic precipitation variability and gap-filling radar potential in Little Cottonwood Canyon, Utah. *Wea. Forecasting*, **29**, 912–935, <https://doi.org/10.1175/WAF-D-13-00129.1>.
- Chandrasekar, V., S. Lim, and E. Gorgucci, 2006: Simulation of X-band rainfall observations from S-band radar data. *J. Atmos. Oceanic Technol.*, **23**, 1195–1205, <https://doi.org/10.1175/JTECH1909.1>.
- , and Coauthors, 2013: The CASA Dallas Fort Worth remote sensing network ICT for urban disaster mitigation. *Geophysical Research Abstracts*, Vol. 15, Abstract EGU2013-6351-1, <http://meetingorganizer.copernicus.org/EGU2013/EGU2013-6351-1.pdf>.
- DeVoor, G. A., 2004: High impact sub-advisory snow events: The need to effectively communicate the threat of short duration high intensity snowfall. *20th Conf. on Weather Analysis and Forecasting/16th Conf. on Numerical Weather Prediction*, Seattle, WA, Amer. Meteor. Soc., P10.2, <http://ams.confex.com/ams/pdfpapers/68261.pdf>.
- Forbes, G. S., and J. H. Merritt, 1984: Mesoscale vortices over the Great Lakes in wintertime. *Mon. Wea. Rev.*, **112**, 377–381, [https://doi.org/10.1175/1520-0493\(1984\)112<0377:MVOTGL>2.0.CO;2](https://doi.org/10.1175/1520-0493(1984)112<0377:MVOTGL>2.0.CO;2).
- Friedrich, K., D. E. Kingsmill, and C. R. Young, 2005: Misocyclone characteristics along Florida gust fronts during CaPE. *Mon. Wea. Rev.*, **133**, 3345–3367, <https://doi.org/10.1175/MWR3040.1>.
- Helmus, J. J., and S. M. Collis, 2016: The Python ARM Radar Toolkit (Py-ART), a library for working with weather radar data in the Python programming language. *J. Open Res. Software*, **4**, e25, <https://doi.org/10.5334/jors.119>.
- Horel, J., and Coauthors, 2002: Mesowest: Cooperative Mesonets in the western United States. *Bull. Amer. Meteor. Soc.*, **83**, 211–225, [https://doi.org/10.1175/1520-0477\(2002\)083<0211:MCMITW>2.3.CO;2](https://doi.org/10.1175/1520-0477(2002)083<0211:MCMITW>2.3.CO;2).
- Inoue, H. Y., and Coauthors, 2011: Finescale Doppler radar observation of a tornado and low-level misocyclones within a winter storm in the Japan Sea coastal region. *Mon. Wea. Rev.*, **139**, 351–369, <https://doi.org/10.1175/2010MWR3247.1>.
- Jorgensen, D. P., M. N. Hanshaw, K. M. Schmidt, J. L. Laber, D. M. Staley, J. W. Kean, and P. J. Restrepo, 2011: Value of a dual-polarized gap-filling radar in support of southern California post-fire debris-flow warnings. *J. Hydrometeorol.*, **12**, 1581–1595, <https://doi.org/10.1175/JHM-D-11-05.1>.
- Junyent, F., and V. Chandrasekar, 2016: An examination of precipitation using CSU–CHILL dual-wavelength, dual-polarization radar observations. *J. Atmos. Oceanic Technol.*, **33**, 313–329, <https://doi.org/10.1175/JTECH-D-14-00229.1>.
- Knapp, K. R., 2008: Scientific data stewardship of International Satellite Cloud Climatology Project B1 global geostationary observations. *J. Appl. Remote Sens.*, **2**, 023548, <https://doi.org/10.1117/1.3043461>.
- Lakshmanan, V., T. Smith, K. Hondl, G. J. Stumpf, and A. Witt, 2006: A real-time, three-dimensional, rapidly updating, heterogeneous radar merger technique for reflectivity, velocity, and derived products. *Wea. Forecasting*, **21**, 802–823, <https://doi.org/10.1175/WAF942.1>.

- Loisel, J., 1909: Squalls and thunderstorms. *Mon. Wea. Rev.*, **37**, 237–239, [https://doi.org/10.1175/1520-0493\(1909\)37\[237:SAT\]2.0.CO;2](https://doi.org/10.1175/1520-0493(1909)37[237:SAT]2.0.CO;2).
- Lundstedt, W., 1993: A method to forecast wintertime instability and non-lake effect snow squalls across northern New England. NWS Eastern Region Tech. Attach. 93-11A, 13 pp.
- Maddox, R. A., J. Zhang, J. J. Gourley, and K. W. Howard, 2002: Weather radar coverage over the contiguous United States. *Wea. Forecasting*, **17**, 927–934, [https://doi.org/10.1175/1520-0434\(2002\)017<0927:WRCOTC>2.0.CO;2](https://doi.org/10.1175/1520-0434(2002)017<0927:WRCOTC>2.0.CO;2).
- Matrosov, S. Y., R. Cifelli, P. C. Kennedy, S. W. Nesbitt, S. A. Rutledge, V. N. Bringi, and B. E. Martner, 2006: A comparative study of rainfall retrievals based on specific differential phase shifts at X- and S-band radar frequencies. *J. Atmos. Oceanic Technol.*, **23**, 952–963, <https://doi.org/10.1175/JTECH1887.1>.
- , C. Campbell, D. Kingsmill, and E. Sukovich, 2009: Assessing snowfall rates from X-band radar reflectivity measurements. *J. Atmos. Oceanic Technol.*, **26**, 2324–2339, <https://doi.org/10.1175/2009JTECHA1238.1>.
- McLaughlin, D., and Coauthors, 2009: Short-wavelength technology and the potential for distributed networks of small radar systems. *Bull. Amer. Meteor. Soc.*, **90**, 1797–1818, <https://doi.org/10.1175/2009BAMS2507.1>.
- Milrad, S. M., J. R. Gyakum, E. H. Atallah, and J. F. Smith, 2011: A diagnostic examination of the eastern Ontario and western Quebec wintertime convection event of 28 January 2010. *Wea. Forecasting*, **26**, 301–318, <https://doi.org/10.1175/2010WAF2222432.1>.
- , —, K. Lombardo, and E. H. Atallah, 2014: On the dynamics, thermodynamics, and forecast model evaluation of two snow-burst events in southern Alberta. *Wea. Forecasting*, **29**, 725–749, <https://doi.org/10.1175/WAF-D-13-00099.1>.
- Mulholland, J. P., J. Frame, S. W. Nesbitt, S. M. Steiger, K. A. Kosiba, and J. Wurman, 2017: Observations of misovortices within a long-lake-axis-parallel lake-effect snowband during the OWLeS project. *Mon. Wea. Rev.*, **145**, 3265–3291, <https://doi.org/10.1175/MWR-D-16-0430.1>.
- NCDC, 2018: Record of climatological observations, station: Alamosa San Luis Valley Regional Airport, CO, US USW00023061. NCDC Climate Data Online, accessed 23 January 2018, <https://www.ncdc.noaa.gov/cdo-web/>.
- NRC, 1995: *Assessment of NEXRAD Coverage and Associated Weather Services*. National Academy Press, 104 pp.
- NWS, 2017: Service change notice 17-112 updated. NOAA/NWS, accessed 1 November 2017, [http://www.nws.noaa.gov/os/notification/scn17-112snow\\_dustaaa.htm](http://www.nws.noaa.gov/os/notification/scn17-112snow_dustaaa.htm).
- Pease, S. R., W. A. Lyons, C. S. Keen, and M. Hjelmfelt, 1988: Mesoscale spiral vortex embedded within a Lake Michigan snow squall band: High resolution satellite observations and numerical model simulations. *Mon. Wea. Rev.*, **116**, 1374–1380, [https://doi.org/10.1175/1520-0493\(1988\)116<1374:MSVEWA>2.0.CO;2](https://doi.org/10.1175/1520-0493(1988)116<1374:MSVEWA>2.0.CO;2).
- Pettegrew, B. P., P. S. Market, R. A. Wolf, R. L. Holle, and N. W. S. Demetriades, 2009: A case study of severe winter convection in the Midwest. *Wea. Forecasting*, **24**, 121–139, <https://doi.org/10.1175/2008WAF2007103.1>.
- Schultz, D. M., and J. A. Knox, 2007: Banded convection caused by frontogenesis in a conditionally, symmetrically, and inertially unstable environment. *Mon. Wea. Rev.*, **135**, 2095–2109, <https://doi.org/10.1175/MWR3400.1>.
- Schumacher, R. S., D. M. Schultz, and J. A. Knox, 2010: Convective snowbands downstream of the Rocky Mountains in an environment with conditional, dry symmetric, and inertial instabilities. *Mon. Wea. Rev.*, **138**, 4416–4438, <https://doi.org/10.1175/2010MWR3334.1>.
- Siggia, A. D., and R. E. Passarelli Jr., 2004: Gaussian model adaptive processing (GMAP) for improved ground clutter cancellation and moment calculation. *Proc. Third European Conference on Radar Meteorology*, Visby, Sweden, ERAD, 67–73, [https://www.copernicus.org/erad/2004/online/ERAD04\\_P\\_67.pdf](https://www.copernicus.org/erad/2004/online/ERAD04_P_67.pdf).
- Smith, T. L., S. G. Benjamin, J. M. Brown, S. Weygandt, T. Smirnova, and B. Schwartz, 2008: Convection forecasts from the hourly updated, 3-km High Resolution Rapid Refresh (HRRR) model. *24th Conf. on Severe Local Storms*, Savannah, GA, Amer. Meteor. Soc., 11.1, [https://ams.confex.com/ams/24SLS/techprogram/paper\\_142055.htm](https://ams.confex.com/ams/24SLS/techprogram/paper_142055.htm).
- Steiger, S. M., and Coauthors, 2013: Circulations, bounded weak echo regions, and horizontal vortices observed within long-lake-axis-parallel-lake-effect storms by the Doppler on Wheels. *Mon. Wea. Rev.*, **141**, 2821–2840, <https://doi.org/10.1175/MWR-D-12-00226.1>.
- Wilson, J. W., and W. E. Schreiber, 1986: Initiation of convective storms at radar-observed boundary-layer convergence lines. *Mon. Wea. Rev.*, **114**, 2516–2536, [https://doi.org/10.1175/1520-0493\(1986\)114<2516:IOCSAR>2.0.CO;2](https://doi.org/10.1175/1520-0493(1986)114<2516:IOCSAR>2.0.CO;2).
- Zhang, J., and Coauthors, 2016: Multi-Radar Multi-Sensor (MRMS) quantitative precipitation estimation: Initial operating capabilities. *Bull. Amer. Meteor. Soc.*, **97**, 621–638, <https://doi.org/10.1175/BAMS-D-14-00174.1>.